

Article

Z-Scheme Heterojunction of SnS₂/Bi₂WO₆ for Photoreduction of CO₂ to 100% Alcohol Products by Promoting the Separation of Photogenerated Charges

Yong Xu , Juanjuan Yu, Jianfei Long, Lingxiao Tu, Weili Dai * and Lixia Yang

Key Laboratory of Jiangxi Province for Persistent Pollutants Control and Resources Recycle, School of Environmental and Chemical Engineering, Nanchang Hangkong University, Nanchang 330063, China; xu_yong001@163.com (Y.X.); qddxhjh_1@sina.com (J.Y.); 15007047545@139.com (J.L.); 2002085700109@stu.nchu.edu.cn (L.T.); zgay20080808@126.com (L.Y.)

* Correspondence: wldai81@126.com

Abstract: Using sunlight to convert CO₂ into solar fuel is an ideal solution to both global warming and the energy crisis. The construction of direct Z-scheme heterojunctions is an effective method to overcome the shortcomings of single-component or conventional heterogeneous photocatalysts for photocatalytic CO₂ (carbon dioxide) reduction. In this work, a composite photocatalyst of narrow-gap SnS₂ and stable oxide Bi₂WO₆ were prepared by a simple hydrothermal method. The combination of Bi₂WO₆ and SnS₂ narrows the bandgap, thereby broadening the absorption edge and increasing the absorption intensity of visible light. Photoluminescence, transient photocurrent, and electrochemical impedance showed that the coupling of SnS₂ and Bi₂WO₆ enhanced the efficiency of photogenerated charge separation. The experimental results show that the electron transfer in the Z-scheme heterojunction of SnS₂/Bi₂WO₆ enables the CO₂ reduction reactions to take place. The photocatalytic reduction of CO₂ is carried out in pure water phase without electron donor, and the products are only methanol and ethanol. By constructing a Z-scheme heterojunction, the photocatalytic activity of the SnS₂/Bi₂WO₆ composite was improved to 3.3 times that of pure SnS₂.

Keywords: Bi₂WO₆; SnS₂; photocatalytic CO₂ reduction; charge separation; liquid phase products



Citation: Xu, Y.; Yu, J.; Long, J.; Tu, L.; Dai, W.; Yang, L. Z-Scheme Heterojunction of SnS₂/Bi₂WO₆ for Photoreduction of CO₂ to 100% Alcohol Products by Promoting the Separation of Photogenerated Charges. *Nanomaterials* **2022**, *12*, 2030. <https://doi.org/10.3390/nano12122030>

Academic Editor: Detlef W. Bahnemann

Received: 27 April 2022

Accepted: 9 June 2022

Published: 13 June 2022

Publisher's Note: MDPI stays neutral with regard to jurisdictional claims in published maps and institutional affiliations.



Copyright: © 2022 by the authors. Licensee MDPI, Basel, Switzerland. This article is an open access article distributed under the terms and conditions of the Creative Commons Attribution (CC BY) license (<https://creativecommons.org/licenses/by/4.0/>).

1. Introduction

The fossil fuels dilemma has become a serious issue that must be confronted and tried to solve, especially for the demand of industrial development in today's society [1–3]. Inspired by natural photosynthesis, the conversion of CO₂ into renewable energy driven by light is widely claimed to be the most promising and environmentally friendly way to deal with the global greenhouse effect [4–6]. Although a great deal of effort has been made to transform CO₂ into valuable chemicals, it is rarely reported that the reduction products are alcohol products with high selectivity [5,7]. More importantly, C₂ hydrocarbons are hard to form because it is difficult for C-C coupling reaction to occur and more electrons and protons are needed to participate in the reaction. Another important issue is that semiconductor catalysts suffer from the sluggish charge separation efficiency ascribing to the fast recombination of photogenerated electrons and holes during the photoreaction process [8–10].

In order to improve the efficiency of charge separation as well as the durability of photocatalysts, a great many measures have been taken including adding cocatalysts, manufacturing defects or doping elements in the bulk materials, forming heterojunction, and so on [11–14]. The construction of heterojunction can not only improve the light absorption capacity but also enhance the separation efficiency of photogenerated charge. For example, Guo et al. constructed a Z-scheme NiTiO₃/g-C₃N₄ (NT/GCN) photocatalyst by a facile calcination method. In the absence of any sacrificial agent and cocatalyst, the

optimized NT/GCN40 can obtain the highest CH₃OH yield (13.74 $\mu\text{mol}\cdot\text{g}^{-1}\cdot\text{h}^{-1}$), which is almost 3.29 times that of g-C₃N₄ [15]. Wang et al. designed and fabricated 0D/2D direct Z-scheme heterojunction involving carbonized polymer dots and Bi₄O₅Br₂ nanosheets (CPDs/Bi₄O₅Br₂), which effectively facilitate migration and separation efficiency of photogenerated carriers and retain more negative electron reduction potential of CPDs and more positive hole oxidation potential of Bi₄O₅Br₂. The 8 wt% CPDs/Bi₄O₅Br₂ exhibits the maximal CO production of 132.42 $\mu\text{mol h}^{-1}\text{g}^{-1}$ under Xe lamp irradiation, 5.43-fold higher than that of Bi₄O₅Br₂ nanosheets [16].

SnS₂, as a narrow bandgap semiconductor, is nontoxic and has a bandgap value of 2.2–2.4 eV, which can absorb visible light efficiently. It has a CdI₂-type layered structure, and the force between the layers is the weak van der Waals force. SnS₂ has good chemical thermal stability and oxidation resistance in acidic and neutral solutions, so it has been favored by researchers as a new type of visible light response photocatalyst in recent years [17]. Wu et al. successfully fabricated the SnS-SnS₂ Z-scheme heterostructure with nanosheet framework by post-annealing in a specified atmosphere to partially convert the SnS₂ matrix into SnS. The converted SnS possesses CO₂ adsorption sites with significantly reduced activation energy, which can be used to drive the rate-determining step for efficient CO₂ conversion. The final Z-scheme SnS-SnS₂ heterostructure enhances the photocatalytic activity of CO₂ conversion to C₂ and C₃ hydrocarbons [18]. Wu et al. constructed a novel direct Z-scheme g-C₃N₄/SnS₂ heterojunction by in situ deposition of SnS₂ quantum dots onto the g-C₃N₄ surface by a simple one-step hydrothermal method. The transfer of electrons from g-C₃N₄ to SnS₂ results in the formation of an intra-interface electric field (IEF) between the two semiconductors. Compared with g-C₃N₄ and SnS₂ alone, the g-C₃N₄/SnS₂ hybrid showed better performance of photocatalytic CO₂ reduction [19]. Bi₂WO₆ is a semiconductor multi-element oxide with the bandgap of 2.75 eV, which has a certain response under visible light. Bi₂WO₆ is a direct bandgap semiconductor, the photogenerated electrons and holes generated by illumination have a high probability of direct recombination. So, the photon quantum efficiency is low. In addition, the Bi₂WO₆ material also has a small specific surface area, and the photogenerated charges are easily recombined in the bulk phase, which limits its practical application. According to the energy band matching theory, the energy band positions of SnS₂ and Bi₂WO₆ match each other, and the combination of SnS₂ and Bi₂WO₆ can effectively reduce the recombination of photogenerated electron-hole pairs, thereby achieving the purpose of improving the photocatalytic efficiency. Here, we constructed stable Bi₂WO₆ oxide semiconductors and SnS₂ narrow-bandgap semiconductors as Z-scheme heterojunctions to improve the separation efficiency of photogenerated electrons and holes, thereby enhancing the photocatalytic activity. We also expanded the application of SnS₂/Bi₂WO₆ in photocatalytic reduction of CO₂ and obtained 100% alcohol.

2. Materials and Methods

2.1. Sample Preparation

2.1.1. Preparation of Flower-like SnS₂

SnCl₄·5H₂O (0.525 g) was dissolved into ethylene glycol (80 mL), and then CH₄N₂S (thiourea, 0.609 g) was added. The above solution was stirred until dissolved, and dispersed uniformly by ultrasonic wave. Then the mixture was transferred into 100 mL of autoclave and the temperature was kept at 180 °C for 18 h. Finally, the product was washed with ethanol and distilled water.

2.1.2. Preparation of SnS₂/Bi₂WO₆

Bi(NO₃)₃·5H₂O (0.485 g) and Na₂WO₄·2H₂O (0.165 g) were dissolved in 10 mL of ethylene glycol solution, respectively. After dissolving, the two solutions were mixed and dispersed by ultrasonic treatment. SnS₂ was dissolved in ethylene glycol (60 mL) solution and sonicated for 30 min, then slowly added dropwise to the above solution. The obtained yellow mixture was transferred into a 100 mL of autoclave, and the temperature was kept

at 160 °C for 24 h. The product was washed three times with ethanol and distilled water, respectively. The mass ratio of SnS₂: Bi₂WO₆ was 0.025:1, 0.05:1, 0.1:1, and 0.15:1, thus the composites were named as SnS₂/Bi₂WO₆-2.5, SnS₂/Bi₂WO₆-5, SnS₂/Bi₂WO₆-10, and SnS₂/Bi₂WO₆-15, respectively.

2.2. Characterization

X-ray diffraction (XRD) patterns of prepared samples were determined on a D/max-3 X-ray diffractometer (Bruker, Germany) using Cu K α radiation ($\lambda = 0.154056 \text{ \AA}$). The detailed surface morphology of catalysts was characterized by employing a Nova Nano SEM450 (FEI, Hillsboro, OR, USA) field-emission scanning electron microscope (SEM) and transmission electron microscopy (TEM) images were obtained with JEOL JEM-2100F (Hitachi, Japan) operated at 200 kV. X-ray photoelectron spectroscopy (XPS) analysis was carried out by a Kratos Axis Ultra DLD spectrometer (VERTEX 70, Bruker, Germany) with a monochromatic Al K α X-ray source. The property about light absorption of catalysts were determined with a UV-vis spectrophotometer (Hitachi U-3900H, Tokyo, Japan). Photoluminescence (PL) spectra were obtained using a fluorescence spectrophotometer (Hitachi F-7000, Tokyo, Japan). Transient spectra of the testing samples were recorded with time-resolved fluorescence spectroscopy (Edinburgh, Scotland, FS5).

2.3. Photoelectrochemical Measurements

The transient photocurrent response, EIS and Mott–Schottky curves were carried out on the electrochemical workstation (CHI660E, Shanghai) in a standard three-electrode system with the Pt mesh as the counter electrode, the Ag/AgCl (saturated KCl) as the reference electrode, and the sample loaded photoelectrode as the working electrode in 0.1 M Na₂SO₄ aqueous solution (electrolyte solution) at room temperature. The distance between the counter electrode and the working electrode is 2 cm. Indium tin oxide (ITO) with a 1 cm \times 1 cm area photocatalyst was used as the working electrode. The photocurrent measurement of the photocatalyst is measured by several switching cycles of light irradiated by a 300 W xenon lamp (using a 420 nm cut-off filter).

The photoelectrode in this system is prepared as follows: 10 mg of powder sample was dispersed in 0.2 mL of a mixed solution of ethanol and H₂O (H₂O:ethanol = 1:1 *v/v*), then 5 μ L of Nafion solution was added, and the mixture was sonicated for several minutes. Finally, the obtained slurry was coated on an ITO glass substrate in an area of 1 \times 1 cm.

2.4. Photocatalytic CO₂ Reduction

Light-driven reduction of CO₂ was performed in a closed 200 mL quartz glass reactor containing 50 mL of ultrapure water and 0.05 g of photocatalyst at atmospheric pressure. A 300 W Xe arc lamp (PLS-SXE300, Beijing, China) with a 420 nm cut-off filter was positioned 5 cm above the reactor as a visible light source. Before irradiation, high purity CO₂ gas (99.995%) was bubbled into above suspension for 30 min to expel air and dissolved oxygen. During the whole catalytic process, CO₂ gas was bubbled into the solution at a rate of 50 mL per minute. Since the efficiency in photocatalytic reduction of CO₂ is dependent on both the solubility in water and reaction temperature, 4 °C is optimal for this reaction by considering the trade-off between solubility and temperature. The yields of obtained alcohols were determined by sampling the suspension (1 mL) every hour and filtering it with a specific membrane to remove the solid catalysts. The aimed products such as methanol and ethanol were quantitatively monitored with Agilent Technologies 7890A gas chromatography (Shanghai China, FID detector, DB-WAX column). The detailed diagram of the catalytic reaction device is shown in Figure S1.

3. Results

3.1. Characterization of Materials

Figure 1 shows the XRD patterns of pure SnS₂, Bi₂WO₆ and the composite materials with different mass ratios. The pattern of unmodified Bi₂WO₆ suggests all the diffraction

peaks are indexed to the orthorhombic phase (JCPDS No. 39-0256). The main diffraction peaks at 28.3° , 32.8° , 47.0° , and 55.9° correspond to the crystal planes of (131), (200), (260), and (133), respectively. Bi_2WO_6 has a larger half-width value, and it can be inferred that Bi_2WO_6 has a small grain size, which can provide more reactive sites. The pure phase of SnS_2 mainly has six diffraction peaks, which are consistent with the (001), (100), (101), (102), (110), and (111) planes of the standard card (No. 23-0677). With the increase of the molar ratio of SnS_2 , the diffraction peaks of (101) and (111) crystal planes of SnS_2 gradually appeared. Since the diffraction peak of SnS_2 in the composite material is not obvious, the amount of SnS_2 was increased to 50%, and the obtained XRD patterns are shown in Figure S2. The diffraction peaks of the material with 50% content of SnS_2 become relatively obvious, especially the diffraction peaks around 15° and 50° . This is due to the different degree of crystallization of materials SnS_2 and Bi_2WO_6 , which leads to the obvious difference in the intensity of their diffraction peaks. When the two are combined, the diffraction peaks belonging to SnS_2 will be easily masked by Bi_2WO_6 , especially the peaks near the strong diffraction peaks at 28.3° and 32.6° . Therefore, this leads to masking of the two strongest diffraction peaks near these positions in SnS_2 . The half-peak width of (131) composite is slightly larger than that of pure Bi_2WO_6 (Figure 1). This phenomenon shows that during the hydrothermal process, due to the interaction between the two materials, the single material will be less likely to aggregate, resulting in a slight decrease in the crystallinity of the material [20]. The BET test in Figure S3 shows that the specific surface areas of Bi_2WO_6 and $\text{SnS}_2/\text{Bi}_2\text{WO}_6$ -10 are 25.70 and 37.13 m^2/g , respectively, which indicates that the specific surface area of the composite is significantly increased, while the pore size is slightly reduced.

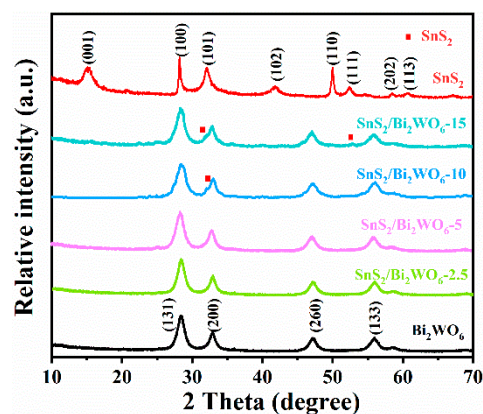


Figure 1. XRD patterns of prepared materials.

The flower-like SnS_2 spheres were prepared by hydrothermal method, as shown in Figure 2a, the diameter distribution ranges from 2 μm to 5 μm . According to Figure 2b, it can be seen more clearly that the spherical SnS_2 is formed by self-assembly with regular two-dimensional nanosheets. Moreover, the reaction process may be due to the adsorption of ethylene glycol on the precursors of SnS_2 , then the intermolecular force as well as crystal growth orientation make the nanosheets self-assemble into the flower-like spheres. The thickness of nanosheets is about 50 nm, besides there are large pores between the nanosheets, which is conducive to the adsorption of CO_2 . This unique porous structure can provide a large number of catalytic active sites and charge transport channels, therefore, the flower-like SnS_2 has higher photocatalytic activity than that of SnS_2 synthesized by traditional method. Figure 2c,d shows the SEM images of the composite $\text{SnS}_2/\text{Bi}_2\text{WO}_6$ -10 obtained by the hydrothermal reaction, while the morphology of nanospheres has no obvious change because of the high dispersion of Bi_2WO_6 . As can be seen from the TEM image (Figure 2e), the SnS_2 spheres consist of staggered nanosheets. Two different lattice distances of 0.278 and 0.315 nm can be observed in the high-resolution TEM (HRTEM) image (Figure 2f), corresponding to the (101) plane of SnS_2 and the (131) plane of Bi_2WO_6 ,

respectively. Figure S4 also shows the HRTEM patterns of SnS₂/Bi₂WO₆-10. In addition, it can be seen from the EDS spectrum of SnS₂/Bi₂WO₆-10 (Figure S5) that there are Bi, W, O, Sn, and S elements in the sample, which indicates that the synthesis method does not introduce other impurity elements, and the ratio of SnS₂ to Bi₂WO₆ is approximately close to the theoretical value (0.1:1).

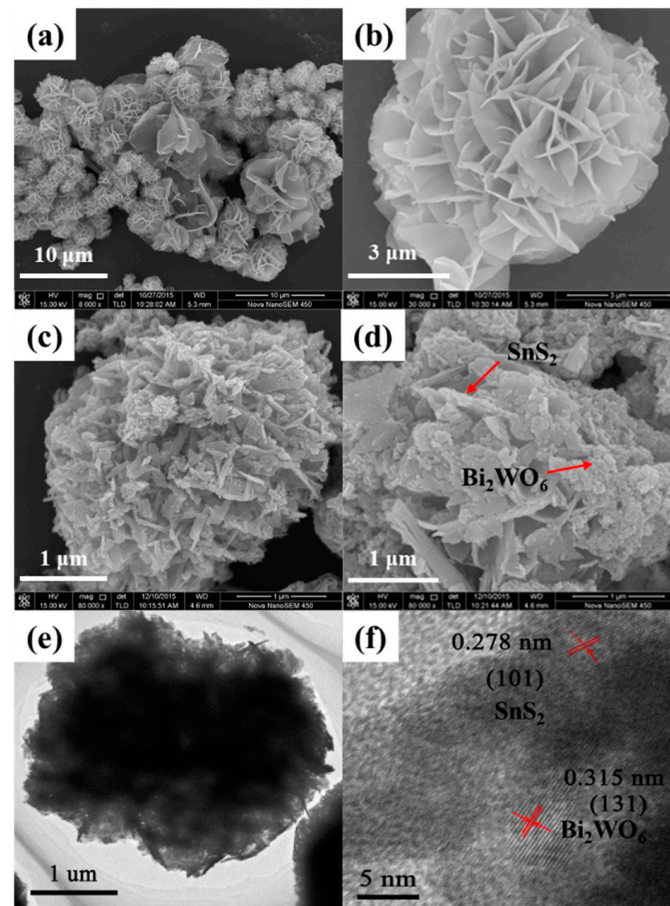


Figure 2. (a,b) SEM images of flower-like SnS₂, (c,d) SEM images of SnS₂/Bi₂WO₆-10, (e,f) TEM images of SnS₂/Bi₂WO₆-10, red arrows and red lines indicate the lattice spacings.

As shown in Figure 3a, an obvious redshift occurs from SnS₂ to SnS₂/Bi₂WO₆-10, which is beneficial to absorb visible light. The combination of SnS₂ and Bi₂WO₆ makes the bandgap narrow, thus broadening the absorption edges and improving the absorption intensity of visible light. The bandgaps are determined using the Tauc/Davis–Mott model described by the equation: $(\alpha h\nu)^{1/n} = A(h\nu - E_g)$ [21]. The exponent *n* denotes the natural properties of the material, and the value of *n* is 0.5 for the direct bandgap. The fitting results (Figure 3b) suggest that the bandgaps of SnS₂, Bi₂WO₆, and SnS₂/Bi₂WO₆-10 are 2.14, 2.75, and 2.26 eV, respectively.

XPS studies were carried out to investigate the surface elemental compositions and chemical states. As depicted in Figure S6, the XPS survey spectrum of SnS₂/Bi₂WO₆-10 indicates that elements of Bi, W, O, Sn, and S exist in the sample. The Bi 4f spectrum of SnS₂/Bi₂WO₆-10 can be deconvoluted into two peaks with spin orbits of Bi 4f_{7/2} and Bi 4f_{5/2}, and the binding energies locate at 158.74 and 164.07 eV assigning to the Bi³⁺ species in Bi₂WO₆ lattice [22]. The peaks located at 34.95 and 37.12 eV are assigned to W 4f_{7/2} and W 4f_{5/2} (Figure 4b), respectively, indicating the oxidation state of W⁶⁺ in SnS₂/Bi₂WO₆-10 composite [23]. Figure 4c displays the high-resolution spectra of Sn 3d, and two characteristic peaks at 486.77 and 495.19 eV ascribe to the inner electrons of Sn 3d_{5/2} and Sn 3d_{3/2} in SnS₂, demonstrating the feature of Sn⁴⁺ species in SnS₂/Bi₂WO₆-10 [24].

The peaks located at 161.67 and 162.53 eV are assigned to S 2p_{3/2} and S 2p_{1/2} (Figure 4d), respectively, indicating the oxidation state of S²⁻ in SnS₂/Bi₂WO₆-10 composite. According to the high-resolution XPS spectra, the binding energies of Bi 4f and W 4f move to the direction of lower binding energy in SnS₂/Bi₂WO₆-10, while the peaks of Sn 3d shift to the direction of larger binding energy. The result suggests that the electron density of Bi and W increases, while the electron density of Sn is reduced, which indicates that there is a strong interaction between Bi₂WO₆ and SnS₂, giving rise to the formation of heterojunction.

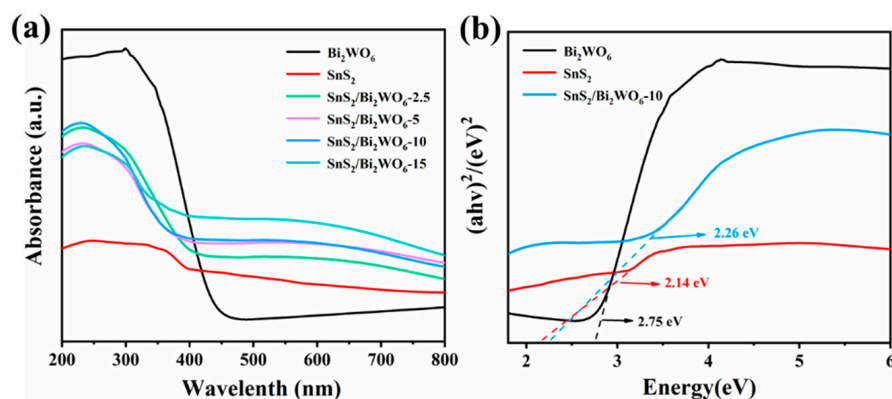


Figure 3. (a) Ultraviolet-visible diffuse reflectance spectra, (b) corresponding plots of $(\alpha hv)^2$ versus energy ($h\nu$) for the bandgap energies.

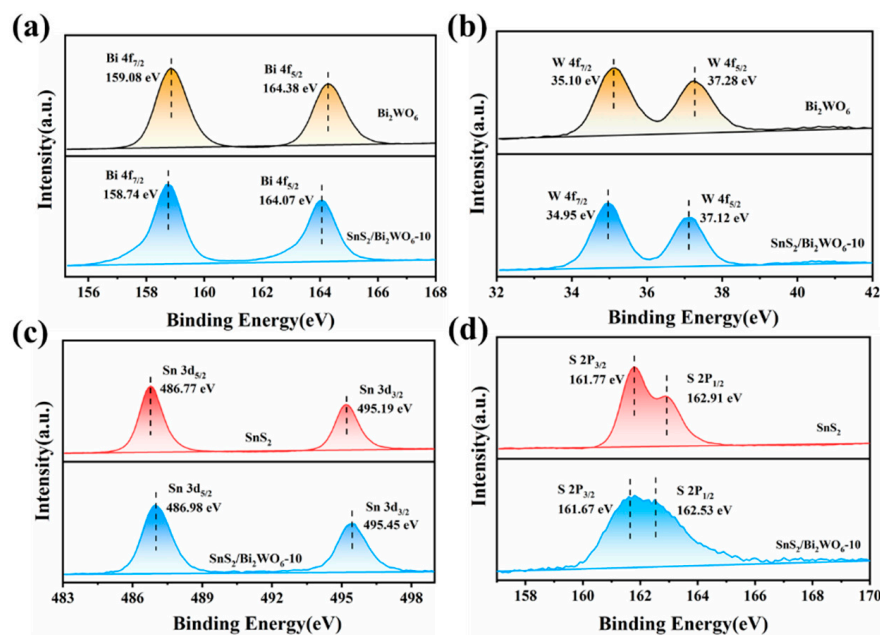


Figure 4. High-resolution XPS spectra of (a) Bi 4f, (b) W 4f, (c) Sn 3d, and (d) S 2p.

3.2. Improvement of Photogenerated Charge Separation

Photoluminescence (PL) is an effective as well as simple method to evaluate the probability of photogenerated electron-hole recombination. Figure 5a shows the fluorescence spectra of SnS₂, Bi₂WO₆, and SnS₂/Bi₂WO₆-10 composite catalysts with different mass ratios, SnS₂ and SnS₂/Bi₂WO₆ with different ratios having similar main peak positions under 300 nm laser excitation. Compared with SnS₂ and Bi₂WO₆ material, the PL intensity of composite materials is significantly reduced due to suppressing the recombination of electron-hole pairs. Therefore, more photoexcited electrons can participate in the reaction of CO₂ reduction. In addition, the time-resolved PL decay spectra of Bi₂WO₆ and SnS₂/Bi₂WO₆-10 are shown in Figure 5b, and the average lifetimes are 1.75 and 0.78 ns,

respectively. This indicates that the addition of SnS₂ will endow the material with effective charge separation, proving the formation of Z-scheme heterojunction between SnS₂ and Bi₂WO₆.

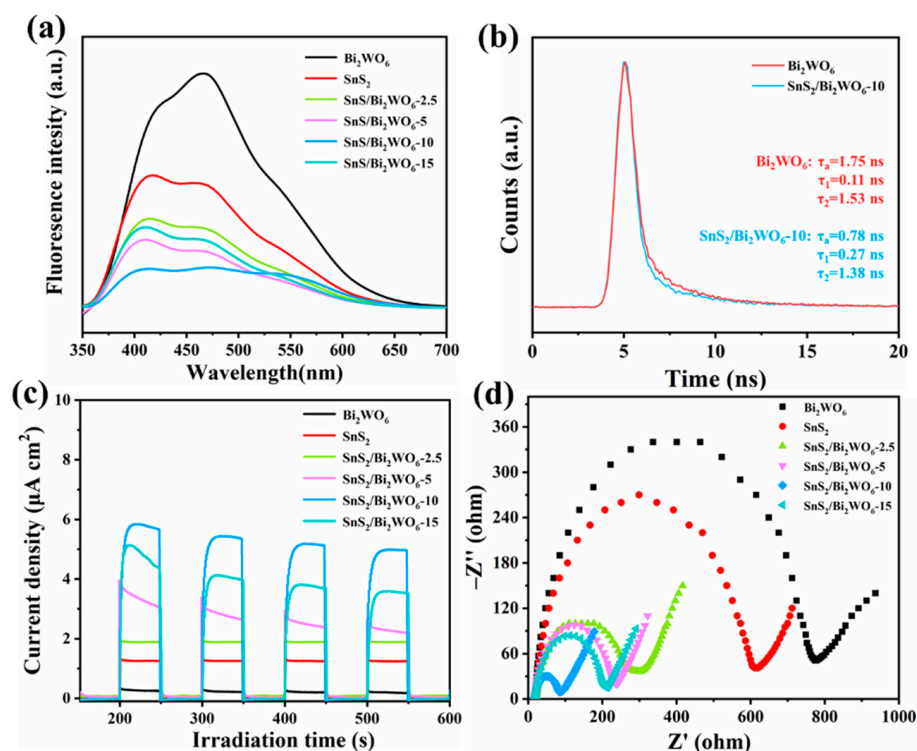


Figure 5. (a) Photoluminescence spectra, (b) time-resolved PL decay spectra, (c) transient photocurrent response, (d) EIS Nyquist plots.

The photocurrent response spectra were tested using a three-electrode system in the electrolyte of 0.5 M Na₂SO₄. As can be seen in Figure 5c, in the continuous on-off conversion of visible light, the samples show a relatively stable photocurrent curve, indicating the photogenerated electrons are effectively captured by the photoelectrochemical system. The catalyst with the largest photocurrent is SnS₂/Bi₂WO₆-10, which is about four times that of pure phase SnS₂. The composite material of SnS₂/Bi₂WO₆ can effectively accelerate the migration of electrons and prolong the lifetime of photogenerated electrons, thus benefiting for improving the efficiency of photocatalytic reduction of CO₂. Electrochemical impedance spectroscopy (EIS) is presented in Figure 5d, the smaller the radius, the faster the charge transfer on the surface of electrode [25]. From the photocurrent response and EIS spectra, we can see that the Z-scheme heterojunction interface formed by an appropriate amount of SnS₂ and Bi₂WO₆ will facilitate the separation and transport of photogenerated charges. However, when the content of SnS₂ is further increased, the sheet-like morphology of SnS₂ will cover Bi₂WO₆ nanoparticles, resulting in poor light absorption. In addition, SnS₂ is prone to recombination of photogenerated electrons and holes due to its narrow bandgap. Therefore, the photocurrent of SnS₂/Bi₂WO₆-15 is lower than that of SnS₂/Bi₂WO₆-10. While the impedance of SnS₂/Bi₂WO₆-15 is higher than that of SnS₂/Bi₂WO₆-10. It can be seen that the radius of SnS₂/Bi₂WO₆-10 in all materials is the smallest, which confirms that SnS₂/Bi₂WO₆-10 possesses an interface that can accelerate the charge transfer, in accordance with the results of PL and photocurrent. At the same time, the Z-scheme heterojunction interface formed with an appropriate amount of SnS₂ and Bi₂WO₆ will facilitate the separation and transport of photogenerated charges. However, when the content of SnS₂ is further increased, the sheet-like morphology of SnS₂ will cover Bi₂WO₆ nanoparticles, resulting in poor light absorption. In addition, SnS₂ is prone to recombination of photogenerated electrons and holes due to its narrow bandgap.

3.3. Photochemical Reduction of CO₂

Photoreduction of CO₂ was performed in a closed 200 mL quartz glass reactor containing 50 mL of ultrapure water saturated with CO₂ and 50 mg of prepared photocatalysts under the irradiation of visible light. After 4 h of photoreaction, only methanol and ethanol were detected as the final products. As presented in Figure 6, with the increase of SnS₂ in the composites, the yields of methanol and ethanol first increase and then decrease. When the amount of SnS₂ reaches 10%, the composite photocatalyst shows the highest catalytic activity. The production rate of methanol and ethanol is 50.2 μmol g⁻¹ and 19.7 μmol g⁻¹ in 4 h respectively, which is nearly 3.3 times that of pure SnS₂, according to the number of transferred electrons. The yields of methanol and ethanol are shown in Table 1. Moreover, the photocatalytic performance of SnS₂/Bi₂WO₆-10 is superior to that of similar photocatalysts reported in other literature (Table S1). The photocatalytic performance starts to decline with further increase in the amount of SnS₂, this conclusion is in line with the results of PL, photocurrent, and EIS. When the amount of SnS₂ reaches a certain level, the catalytic ability drops suddenly, which implies that the excessive SnS₂ is not conducive to the timely transfer of photogenerated electrons to Bi₂WO₆ through Z-scheme heterojunction. In addition, it is worth mentioning that the conduction band (CB) reduction potential of Bi₂WO₆ is theoretically insufficient to directly reduce CO₂ to alcohols. However, after CO₂ is dissolved into water to form CO₃²⁻ and other species, the reduction potential is sufficient to reduce carbonate species to alcohols [26].

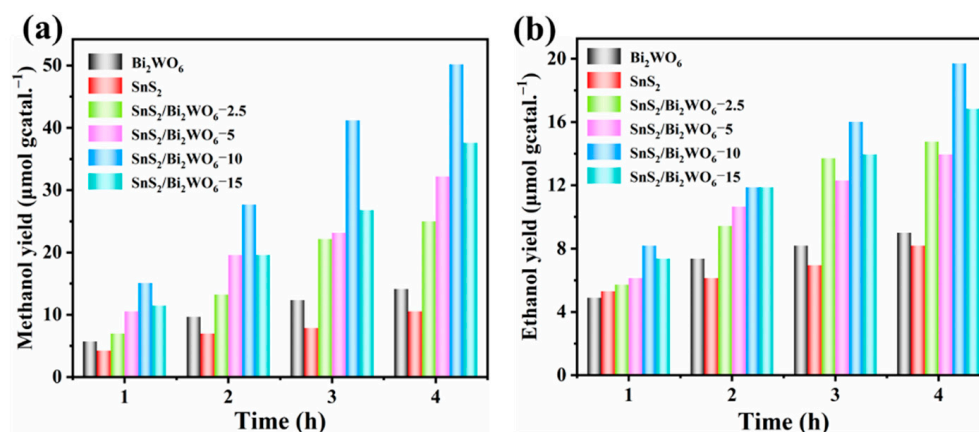


Figure 6. Time dependence of yields of (a) methanol and (b) ethanol during photoreduction of CO₂.

Table 1. 4 h yield of methanol and ethanol.

Sample	Yield of Methanol (μmol g ⁻¹)	Yield of Ethanol (μmol g ⁻¹)
Bi ₂ WO ₆	14.11	9.00
SnS ₂	10.55	8.18
SnS ₂ /Bi ₂ WO ₆ -2.5	24.97	14.76
SnS ₂ /Bi ₂ WO ₆ -5	32.18	13.94
SnS ₂ /Bi ₂ WO ₆ -10	50.20	19.70
SnS ₂ /Bi ₂ WO ₆ -15	37.58	16.82

The control experiments showed that the products of methanol and ethanol were not detected in the dark or without catalyst, indicating that the light source and catalyst are essential factors for photochemical reduction of CO₂. No carbon-containing product was detected when CO₂ was replaced by N₂, suggesting CO₂ is also a necessary condition for CO₂ photosplitting. In other words, the element of C in the products is derived from the reactant CO₂. In order to investigate the stability of SnS₂/Bi₂WO₆-10, the cycling experiment was carried out. At the end of each cycle, the reaction suspension was centrifuged, after washing with distilled water for several times, it was dried in vacuum at 60 °C for next

run. As shown in Figure S7, the catalytic performance of SnS₂/Bi₂WO₆-10 shows a slight decrease after four consecutive cycles. Figure S8 is the XRD pattern of SnS₂/Bi₂WO₆-10 after four cycles, which is consistent with fresh one, further proving its good stability.

Figure 7a shows the Mott–Schottky plots of flower-like SnS₂ and Bi₂WO₆ at voltages from −1.0 to 1.0 V. Classified according to the conductive properties of semiconductors, flower-shaped spherical SnS₂ and Bi₂WO₆ nanoparticle materials belong to n-type semiconductors. The flat band potential (V_{fb}) of SnS₂ is −0.44 V vs. SCE (saturated calomel electrode), which is equivalent to −0.20 V vs. NHE (normal hydrogen electrode), so the CB potential (V_{CB}) of flower-shaped spherical SnS₂ can be calculated to be −0.40 V. The V_{fb} of Bi₂WO₆ is −0.32 V vs. SCE, which is equivalent to −0.080 V vs. NHE, so the V_{CB} of Bi₂WO₆ can be calculated to be −0.280 V. According to the photocatalytic theory [27], the potentials for photocatalytic reduction of CO₂ to methanol and ethanol are −0.38 V and −0.33 V (vs. NHE, pH = 7.00), respectively. Therefore, the Z-scheme heterojunction composed of SnS₂ and Bi₂WO₆ has sufficient reduction ability to reduce CO₂ to methanol and ethanol. In addition, the surface photovoltage test (Figure 7b) further shows that the SnS₂/Bi₂WO₆-10 has higher surface photovoltage after photoexcitation, thus more photogenerated electrons will transfer to the surface active sites, and the photoreduction efficiency of CO₂ is significantly improved compared to pure phase of SnS₂ and Bi₂WO₆.

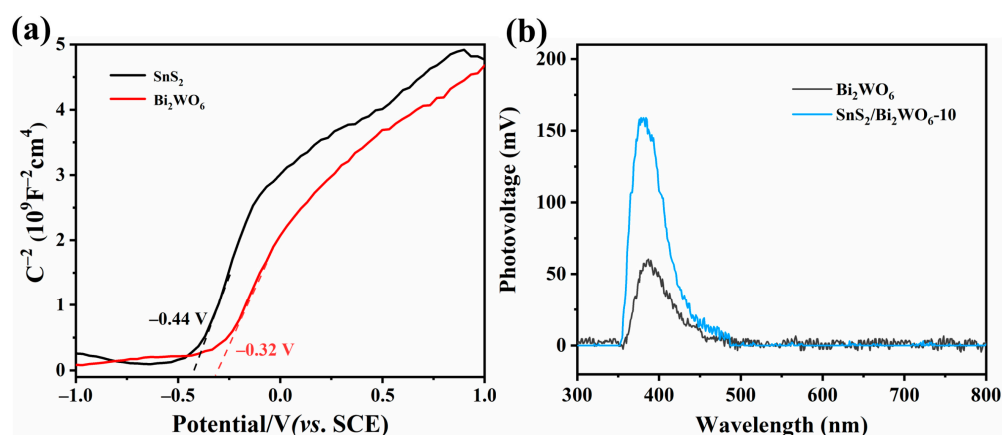
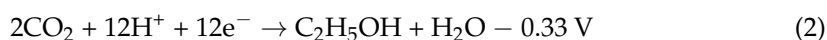
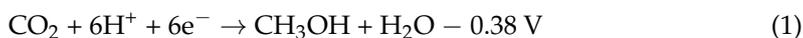


Figure 7. Mott–Schottky plot of (a) Bi₂WO₆ and SnS₂, (b) surface photovoltage spectra.

Based on the above experimental results and discussion, the possible reaction mechanism is as follows: electrons (e^-) in the valence bands (VBs) of SnS₂ and Bi₂WO₆ are excited and transfer to the CBs under sunlight irradiation, thus leaving the same number of holes (h^+) in the VBs of SnS₂ and Bi₂WO₆. Then, the photogenerated electrons on the CB of Bi₂WO₆ are transferred to the VB of SnS₂, subsequently the electrons are excited to the CB of SnS₂. Therefore, the photogenerated electrons and holes of the SnS₂/Bi₂WO₆ photocatalyst are effectively separated by constructing Z-scheme heterojunction. Based on Equations (1)–(3) [28], the electrons on the CB of SnS₂ have enough reduction ability to reduce the CO₂ to methanol and ethanol. This is further demonstrated by Pt photodeposition experiment on SnS₂/Bi₂WO₆-10 (Figure S9). In addition, the Bi₂WO₆ sphere is composed of intricate nanosheets, so some intermediates ($\cdot\text{CH}_3$, $\cdot\text{OCH}_3$) may not be converted into methanol immediately, and the dimerization reaction takes place, and finally ethanol can be formed (Figure 8).



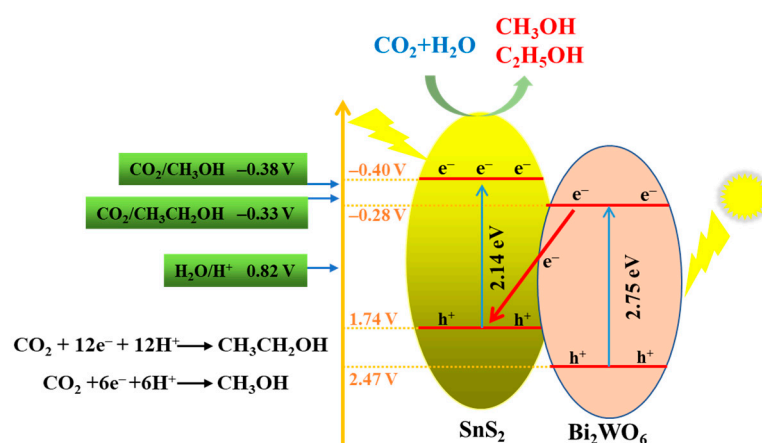


Figure 8. Mechanism diagram of photocatalytic reaction.

4. Conclusions

Here, flower-like SnS₂ microspheres were successfully prepared by hydrothermal method, and SnS₂/Bi₂WO₆ composites with different mass ratios were synthesized. Among them, SnS₂/Bi₂WO₆-10 exhibited the highest catalytic activity in the photochemical reduction of CO₂ without sacrificial agent, and only methanol and ethanol were detected as reduction products. The improvement of catalytic activity is attributed to the formation of Z-scheme heterojunction between SnS₂ and Bi₂WO₆. Under sunlight irradiation, the photo-generated electrons in the CB of Bi₂WO₆ will be transferred to the VB of SnS₂. Therefore, the photogenerated electrons and holes of the SnS₂/Bi₂WO₆ photocatalyst are effectively separated, which effectively inhibits the recombination of photogenerated electron-hole pairs and expands the light absorption range. Finally, the yield of CO₂ photoreduction to alcohol products was 3.3 times higher than that of SnS₂ in pure water.

Supplementary Materials: The following supporting information can be downloaded at: <https://www.mdpi.com/article/10.3390/nano12122030/s1>. Figure S1: Reaction device diagram. Figure S2: XRD spectra of SnS₂/Bi₂WO₆-50. Figure S3: (a) N₂ adsorption-desorption isotherms, and (b) pore size distribution profiles of Bi₂WO₆ and SnS₂/Bi₂WO₆-10. Figure S4: HRTEM spectra of SnS₂/Bi₂WO₆-10. Figure S5: EDS spectrum of SnS₂/Bi₂WO₆-10. Figure S6: XPS survey spectra of Bi₂WO₆ and SnS₂/Bi₂WO₆-10. Figure S7: Cycling tests with catalyst SnS₂/Bi₂WO₆-10 for 4 h irradiation. Figure S8: XRD patterns before and after recycling. Figure S9: HRTEM spectra of 1%Pt-SnS₂/Bi₂WO₆-10. Table S1: The comparison of CO₂ photoreduction performance. References [29–35] are cited in the supplementary materials.

Author Contributions: Conceptualization, W.D.; methodology, Y.X.; validation, J.Y. and J.L.; formal analysis, L.T.; investigation, L.Y.; resources, W.D.; data curation, Y.X.; writing—original draft preparation, Y.X.; writing—review and editing, J.L.; visualization, J.Y.; supervision, J.L.; project administration, L.T.; funding acquisition, W.D. All authors have read and agreed to the published version of the manuscript.

Funding: This research was funded by the National Natural Science Foundation of China (Grants 52072165, 51662031, 51720105001, 51938007 and 51868051), and the project funded by China Postdoctoral Science Foundation (2019M653583). We are grateful for the financial support received for the project.

Institutional Review Board Statement: Not applicable.

Informed Consent Statement: Not applicable.

Data Availability Statement: Not applicable.

Conflicts of Interest: The authors declare no conflict of interest.

References

1. Habisreutinger, S.N.; Schmidt-Mende, L.; Stolarczyk, J.K. Photocatalytic reduction of CO₂ on TiO₂ and other semiconductors. *Angew. Chem. Int. Ed.* **2013**, *52*, 7372–7408. [[CrossRef](#)] [[PubMed](#)]
2. Albero, J.; Peng, Y.; García, H. Photocatalytic CO₂ reduction to C₂+ products. *ACS Catal.* **2020**, *10*, 5734–5749. [[CrossRef](#)]
3. Abdullah, H.; Khan, M.M.R.; Ong, H.R.; Yaakob, Z. Modified TiO₂ photocatalyst for CO₂ photocatalytic reduction: An overview. *J. CO₂ Util.* **2017**, *22*, 15–32. [[CrossRef](#)]
4. Prabhu, P.; Jose, V.; Lee, J.M. Heterostructured catalysts for electrocatalytic and photocatalytic carbon dioxide reduction. *Adv. Funct. Mater.* **2020**, *30*, 1910768. [[CrossRef](#)]
5. Fu, J.W.; Jiang, K.X.; Qiu, X.Q.; Yu, J.G.; Liu, M. Product selectivity of photocatalytic CO₂ reduction reactions. *Mater. Today* **2020**, *32*, 222–243. [[CrossRef](#)]
6. Xu, Y.; Mo, J.; Xie, G.Q.; Wang, X.X.; Ding, S.J. The main factor to improve the performance of CoSe₂ for photocatalytic CO₂ reduction: Element doping or phase transformation. *J. Mater. Chem. A* **2020**, *8*, 4457–4463. [[CrossRef](#)]
7. Gao, S.; Lin, Y.; Jiao, X.C.; Sun, Y.F.; Luo, Q.Q.; Zhang, W.H.; Li, D.Q.; Yang, J.L.; Xie, Y. Partially oxidized atomic cobalt layers for carbon dioxide electroreduction to liquid fuel. *Nature* **2016**, *529*, 68–71. [[CrossRef](#)]
8. Zhao, G.X.; Zhou, W.; Sun, Y.B.; Wang, X.K.; Liu, H.M.; Meng, X.G.; Chang, K.; Ye, J.H. Efficient photocatalytic CO₂ reduction over Co(II) species modified CdS in aqueous solution. *Appl. Catal. B Environ.* **2018**, *226*, 252–257. [[CrossRef](#)]
9. Di, J.; Chen, C.; Zhu, C.; Song, P.; Duan, M.L.; Xiong, J.; Long, R.; Xu, M.Z.; Kang, L.X.; Guo, S.S.; et al. Cobalt nitride as a novel cocatalyst to boost photocatalytic CO₂ reduction. *Nano Energy* **2021**, *79*, 105429. [[CrossRef](#)]
10. Bian, J.; Feng, J.N.; Zhang, Z.Q.; Li, Z.J.; Zhang, Y.H.; Liu, Y.D.; Ali, S.; Qu, Y.; Bai, L.L.; Xie, J.J.; et al. Dimension-matched zinc phthalocyanine/BiVO₄ ultrathin nanocomposites for CO₂ reduction as efficient wide-visible-light-driven photocatalysts via a cascade charge transfer. *Angew. Chem. Int. Ed.* **2019**, *58*, 10873–10878. [[CrossRef](#)] [[PubMed](#)]
11. Lingampalli, S.R.; Ayyub, M.M.; Rao, C.N.R. Recent progress in the photocatalytic reduction of carbon dioxide. *ACS Omega* **2017**, *2*, 2740–2748. [[CrossRef](#)]
12. Ou, M.; Tu, W.G.; Yin, S.M.; Xing, W.N.; Wu, S.Y.; Wang, H.J.; Wan, S.P.; Zhong, Q.; Xu, R. Amino-assisted anchoring of CsPbBr₃ perovskite quantum dots on porous g-C₃N₄ for enhanced photocatalytic CO₂ reduction. *Angew. Chem. Int. Ed.* **2018**, *57*, 13570–13574. [[CrossRef](#)]
13. Wu, J.; Li, X.D.; Shi, W.; Ling, P.Q.; Sun, Y.F.; Jiao, X.C.; Gao, S.; Liang, L.; Xu, J.Q.; Yan, W.S.; et al. Efficient visible-light-driven CO₂ reduction mediated by defect-engineered BiOBr atomic layers. *Angew. Chem. Int. Ed.* **2018**, *57*, 8719–8723. [[CrossRef](#)]
14. Wang, J.; Xia, T.; Wang, L.; Zheng, X.S.; Qi, Z.M.; Gao, C.; Zhu, J.F.; Li, Z.Q.; Xu, H.X.; Xiong, Y.J. Enabling visible-light-driven selective CO₂ reduction by doping quantum dots: Trapping electrons and suppressing H₂ evolution. *Angew. Chem. Int. Ed.* **2018**, *57*, 16447–16451. [[CrossRef](#)]
15. Guo, H.W.; Wan, S.P.; Wang, Y.A.; Ma, W.H.; Zhong, Q.; Ding, J. Enhanced photocatalytic CO₂ reduction over direct Z-scheme NiTiO₃/g-C₃N₄ nanocomposite promoted by efficient interfacial charge transfer. *Chem. Eng. J.* **2021**, *412*, 128646. [[CrossRef](#)]
16. Wang, B.; Zhao, J.Z.; Chen, H.L.; Weng, Y.X.; Tang, H.; Chen, Z.R.; Zhu, W.S.; She, Y.B.; Xia, J.X.; Li, H.M. Unique Z-scheme carbonized polymer dots/Bi₄O₅Br₂ hybrids for efficiently boosting photocatalytic CO₂ reduction. *Appl. Catal. B* **2021**, *293*, 120182. [[CrossRef](#)]
17. Zhang, Y.C.; Du, Z.N.; Li, S.Y.; Zhang, M. Novel synthesis and high visible light photocatalytic activity of SnS₂ nanoflakes from SnCl₂·2H₂O and S powders. *Appl. Catal. B* **2010**, *91*, 153–159. [[CrossRef](#)]
18. Wu, C.Y.; Lee, C.J.; Yu, Y.H.; Tsao, H.W.; Su, Y.H.; Kaun, C.C.; Chen, J.S.; Wu, J.J. Efficacious CO₂ photoconversion to C₂ and C₃ hydrocarbons on upright SnS–SnS₂ heterojunction nanosheet frameworks. *ACS Appl. Mater. Interfaces* **2021**, *13*, 4984–4992. [[CrossRef](#)]
19. Di, T.M.; Zhu, B.C.; Cheng, B.; Yu, J.G.; Xu, J.S. A direct Z-scheme g-C₃N₄/SnS₂ photocatalyst with superior visible-light CO₂ reduction performance. *J. Catal.* **2017**, *352*, 532–541. [[CrossRef](#)]
20. Zhang, S.Q.; Xiong, W.W.; Long, J.F.; Si, Y.M.; Xu, Y.; Yang, L.X.; Zou, J.P.; Dai, W.L.; Luo, X.B.; Luo, S.L. High-throughput lateral and basal interface in CeO₂@Ti₃C₂T_x: Reverse and synergistic migration of carrier for enhanced photocatalytic CO₂ reduction. *J. Colloid Interface Sci.* **2022**, *615*, 716–724. [[CrossRef](#)]
21. Xu, Y.; Fu, Z.C.; Cao, S.; Chen, Y.; Fu, W.F. Highly selective oxidation of sulfides on a CdS/C₃N₄ catalyst with dioxygen under visible-light irradiation. *Catal. Sci. Technol.* **2017**, *7*, 587–595. [[CrossRef](#)]
22. Nie, Z.P.; Ma, D.K.; Fang, G.Y.; Chen, W.; Huang, S.M. Concave Bi₂WO₆ nanoplates with oxygen vacancies achieving enhanced electrocatalytic oxygen evolution in near-neutral water. *J. Mater. Chem. A* **2016**, *4*, 2438–2444. [[CrossRef](#)]
23. Xiang, Y.H.; Ju, P.; Wang, Y.; Sun, Y.; Zhang, D.; Yu, J.Q. Chemical etching preparation of the Bi₂WO₆/BiOI p–n heterojunction with enhanced photocatalytic antifouling activity under visible light irradiation. *Chem. Eng. J.* **2016**, *288*, 264–275. [[CrossRef](#)]
24. Shown, I.; Samireddi, S.; Chang, Y.C.; Putikam, R.; Chang, P.H.; Sabbah, A.; Fu, F.Y.; Chen, W.F.; Wu, C.I.; Yu, T.Y.; et al. Carbon-doped SnS₂ nanostructure as a high-efficiency solar fuel catalyst under visible light. *Nat. Commun.* **2018**, *9*, 169. [[CrossRef](#)] [[PubMed](#)]
25. Lim, J.; Monllor-Satoca, D.; Jang, J.S.; Lee, S.; Choi, W. Visible light photocatalysis of fullerol-complexed TiO₂ enhanced by Nb doping. *Appl. Catal. B Environ.* **2014**, *152*, 233–240. [[CrossRef](#)]
26. Pan, P.W.; Chen, Y.W. Photocatalytic reduction of carbon dioxide on NiO/InTaO₄ under visible light irradiation. *Catal. Commun.* **2007**, *8*, 1546–1549. [[CrossRef](#)]

27. Li, K.; Peng, B.S.; Peng, T.Y. Recent advances in heterogeneous photocatalytic CO₂ conversion to solar fuels. *ACS Catal.* **2016**, *6*, 7485–7527. [[CrossRef](#)]
28. Dai, W.L.; Long, J.F.; Yang, L.X.; Zhang, S.Q.; Xu, Y.; Luo, X.B.; Zou, J.P.; Luo, S.L. Oxygen migration triggering molybdenum exposure in oxygen vacancy-rich ultra-thin Bi₂MoO₆ nanoflakes: Dual binding sites governing selective CO₂ reduction into liquid hydrocarbons. *J. Energy Chem.* **2021**, *61*, 281–289. [[CrossRef](#)]
29. Dai, W.L.; Yu, J.J.; Xu, H.; Hu, X.; Luo, X.B.; Yang, L.X.; Tu, X.M. Synthesis of hierarchical flower-like Bi₂MoO₆ microspheres as efficient photocatalyst for photoreduction of CO₂ into solar fuels under visible light. *CrystEngComm* **2016**, *18*, 3472–3480. [[CrossRef](#)]
30. Xu, F.; Zhu, B.; Cheng, B.; Yu, J.G.; Xu, J.S. 1D/2D TiO₂/MoS₂ hybrid nanostructures for enhanced photocatalytic CO₂ reduction. *Adv. Opt. Mater.* **2018**, *6*, 1800911. [[CrossRef](#)]
31. Yang, G.; Chen, D.; Ding, H.; Feng, J.; Zhang, J.Z.; Zhu, Y.; Hamid, S.; Bahnemann, D.W. Well-designed 3D ZnIn₂S₄ nanosheets/TiO₂ nanobelts as direct Z-scheme photocatalysts for CO₂ photoreduction into renewable hydrocarbon fuel with high efficiency. *Appl. Catal. B* **2017**, *219*, 611–618. [[CrossRef](#)]
32. Yan, Y.; Yu, Y.; Huang, S.; Yang, Y.; Yang, X.; Yin, S.; Cao, Y. Adjustment and matching of energy band of TiO₂-based photocatalysts by metal ions (Pd, Cu, Mn) for photoreduction of CO₂ into CH₄. *J. Phys. Chem. C* **2017**, *121*, 1089–1098. [[CrossRef](#)]
33. Dai, W.L.; Xu, H.; Yu, J.J.; Hu, X.; Luo, X.B.; Tu, X.M.; Yang, L.X. Photocatalytic reduction of CO₂ into methanol and ethanol over conducting polymers modified Bi₂WO₆ microspheres under visible light. *Appl. Surf. Sci.* **2015**, *798*, 173–180. [[CrossRef](#)]
34. Al-Mhyawi, S.R.; Salam, M.A. Enhancement of photocatalytic activity of Gd(OH)₃ nanoparticles by Pd deposition for reduction of CO₂ to methanol. *J. Photoch. Photobio. A* **2018**, *367*, 89–93. [[CrossRef](#)]
35. Abdullah, H.; Khan, M.R.; Pudukudy, M.; Yaakob, Z.; Ismail, N.A. CeO₂-TiO₂ as a visible light active catalyst for the photoreduction of CO₂ to methanol. *J. Rare Earth.* **2015**, *11*, 1155–1161. [[CrossRef](#)]